

# Examining 22 Years of Ambient Seismic Wavefield at Mount St. Helens

Manuela Köpfli<sup>1</sup> , Marine A. Denolle<sup>1</sup> , Weston A. Thelen<sup>2</sup> , Peter Makus<sup>3,4</sup> , and Stephen D. Malone<sup>1</sup> 

## Abstract

An increase in seismic activity precedes most volcanic eruptions. While event-based forecasting approaches have been successful, some eruptions remain unanticipated, resulting in casualties and damage. Our study leverages the recent advancements in ambient field seismology. We explore features extracted from continuous ambient fields using traditional methods, e.g., PGV, PGA, RMS, RMeS, and Real-time Seismic Amplitude Measurement, and novel methods, e.g., Displacement Seismic Amplitude Ratio and spectral width. In addition, we explore unsupervised learning of higher-order wavelet features using scattering networks. We find that combining all methods was necessary to disentangle the effects of seismic sources from structural changes at Mount St. Helens. Although the ambient wavefield-based approach does not yield additional or more significant precursory signals than event-based methods at Mount St. Helens our study demonstrates that the ambient wavefield provides supplementary information, mainly about structural changes, and complements traditional methods.

The ambient seismic wavefield offers additional insights into long-lasting processes. We find enhanced wave attenuation correlating with geochemical measurements. We interpret this as ongoing structural changes, such as dome growth or the evolution of the volcanic conduit system. On annual and decadal timescales, we interpret seasonal seismic attenuation in the shallow subsurface as groundwater fluctuations, corroborated by observations at the nearby Spirit Lake level. This multimethod approach at Mount St. Helens sheds light on a volcanic system's underlying dynamics and structure.

## Introduction

The 1980–1986 eruption and subsequent dome-building event of Mount St. Helens are among the largest volcanic eruptions in the past century in the United States (Lipman and Mullineaux, 1981). At that time, seismic monitoring of the eruption was carried out on event-triggered recordings of ground shaking (Malone et al., 1981; Endo et al., 1981; Weaver et al., 1981). In 1980, the local seismic network was sparse, and the beginning of volcanic unrest at Mount St. Helens was recorded by only one local seismometer (Malone, 2020). After recognizing the seismic unrest, a

seismometer network was rapidly deployed. However, most data remained saved in event-triggered recordings and a handful of continuous recordings (supplementary information: 1980 Eruption of Mount St. Helens). A more recent dome-forming eruption occurred between 2004 and 2008, further expanding the seismic network.

In addition to seismic data recording, visual observations of the eruptions allowed volcano-seismologists to attribute observed processes to some seismic signals (Christiansen and Peterson, 1981; Scott et al., 2008; Moran et al., 2008b; Matoza et al., 2009; Salzer et al., 2016; Swanson et al., 1983; Chadwick Jr and Swanson, 1989), and most visual observations could be linked to specific seismic recordings. For the initial explosions in the 1980 and 2004 eruptions, the US Geological Survey and the University of Washington issued an eruption warning days before the initial small explosions (Malone et al., 1981; Decker, 1981; Miller et al., 1981; Malone et al., 1983; Swanson et al., 1983; Frenzen and Matarrese, 2008; Driedger et al., 2008; Scott et al.,

1. Earth and Space Sciences, University of Washington, Seattle, WA, USA,

 <https://orcid.org/0000-0000-0000-0001> (MK)  <https://orcid.org/0000-0002-1610-2250> (MA); 2. USGS Cascade Volcano Observatory, Vancouver, WA, USA,

 <https://orcid.org/0000-0003-2534-5577> (WT); 3. German Research Centre for Geosciences GFZ, Potsdam, Germany,  <https://orcid.org/0000-0002-6377-5888> (PM); 4. Freie Universität Berlin, Institute for Geological Sciences, Berlin, Germany,  <https://orcid.org/0000-0002-6377-5888> (PM)

\*Corresponding author: koepflma@uw.edu

© Seismological Society of America

2008). Additionally, many dome-building eruptions were forecasted using observed changes in seismic activity and deformation hours to days before the eruption onset (Malone et al., 1981; Swanson et al., 1983; Qamar et al., 2008). At Mount St. Helens, traditional event-based eruption forecasting was successful because of the release of seismic energy as distinct seismic events during the pre-eruption phase.

One measure of generated seismic energy is Real-time Seismic Amplitude Measurement (RSAM), a time-averaged estimate of absolute amplitude measured continuously in seismograms. RSAM is a basic volcano monitoring tool deployed at many volcanoes because of its ease of implementation and the requirement of only a single seismometer. But some volcanoes (e.g., Kawah Ijen (Indonesia); Ruapehu, and Tongariro (New Zealand); Caudron et al. (2019); Ardid et al. (2022, 2023)) experience much weaker seismicity before eruptions, reducing the effectiveness of traditional event-based forecasting methods. This motivates the development of ambient wavefield methods to study structural changes that precede or follow eruptions.

Changes in the subsurface of volcanoes in various stages can be detected in signals buried in the ambient seismic wavefield. The seismic wavespeed beneath the volcano may change before eruptions, sometimes decreasing (e.g., Brenguier et al., 2008; Olivier et al., 2019; Machacca-Puma et al., 2019; Feng et al., 2020; Caudron et al., 2022a), and sometimes increasing (e.g., Denlinger and Moran, 2014; Yates et al., 2019; Makus et al., 2023), depending on the depth and nature of the process creating the change. In addition, seismic wavespeeds also vary in the absence of volcanic activity according to hydrological conditions, as shown by Sabra et al. (2006); Hotovec-Ellis et al. (2014, 2015); Makus et al. (2024) for Mount St. Helens using coda wave interferometry. But calculating changes in seismic wavespeed requires high computational power.

As an efficient method that can be deployed in real-time, Caudron et al. (2019) proposed to approximate seismic wave attenuation with the Displacement Seismic Amplitude Ratio (DSAR). Seismic wave attenuation also changes during volcanic eruptions due to magma influx or volatile accumulation and becomes generalizable to several volcanoes (Whakaari, Tongariro, and Ruapehu (New Zealand); Mount Veniaminof, and Pavlof Volcano (Alaska, USA); Bezymianny (Kamchatka, Russia) after normalizing (Ardid et al., 2022).

However, changes in seismic wave attenuation and seismic wavespeed suffer from ambiguous source and path effects. The conventional method in array seismology

to find the nature and orientation of seismic sources in the seismic wavefield is beamforming (Rost and Thomas, 2002). Beamforming assumes plane waves at a large source-receiver array distance. However, volcanic signals originate from within a seismic network and can thus not be assumed to be plane waves. Seydoux et al. (2016a) therefore developed a “covariance analysis” to decompose the coherent wavefield into eigenmodes and quantify the degree of localized versus diffuse seismic signals. During volcanic eruptions, the coherence of the wavefield increases due to the stronger and more localized seismic sources, such as periods of volcanic tremor (e.g., Journeau et al. (2020); Soubestre et al. (2021); Caudron et al. (2022a); Maher et al. (2023); Barajas et al. (2023)).

Finally, we tested an unsupervised learning approach which helped identify precursory signals of mass movements (Seydoux et al., 2020), earthquakes (Steinmann et al., 2022a), and cryospheric signals (Jenkins et al., 2021) by clustering features of windowed seismic data.

This study combines event-based, noise-based, and unsupervised learning approaches to disentangle the signature of seismic sources from the structural changes in the continuous seismic wavefield. Using decade-long recordings from the seismic network at Mount St. Helens, we demonstrate that ambient wavefield analysis provides additional insight into structural evolution. Ambient seismic wavefield analysis highlights long-lasting processes such as fluid migration (e.g., magma or groundwater) and allows us to identify a second period of structural changes, as well as a seasonal hydrological pattern. However, traditional event-based methods remain effective in forecasting eruptions of Mount St. Helens.

## Data Availability & Quality

We focused our study on a 18-kilometer radius around Mount St. Helens and considered all active seismic stations for at least one month between 2000 and 2022 (Fig. 1). Our dataset includes data from up to 30 stations (Tab. S1), of which around 10 were recorded simultaneously during the 2004 eruption. The station availability changed quickly, especially during the eruption, due to the destruction and re-establishment of stations affected by eruptions.

Initially, most seismometers were single-component (vertical), short-period instruments with a flat response between 0.8 and 20 Hz, sampled at 100 Hz (UW seismic network). The first permanent 3-component broadband site, with a flat response from 0.008 Hz, sampled at 50 Hz, was installed in 2004, and stations were upgraded and added (CC seismic network).

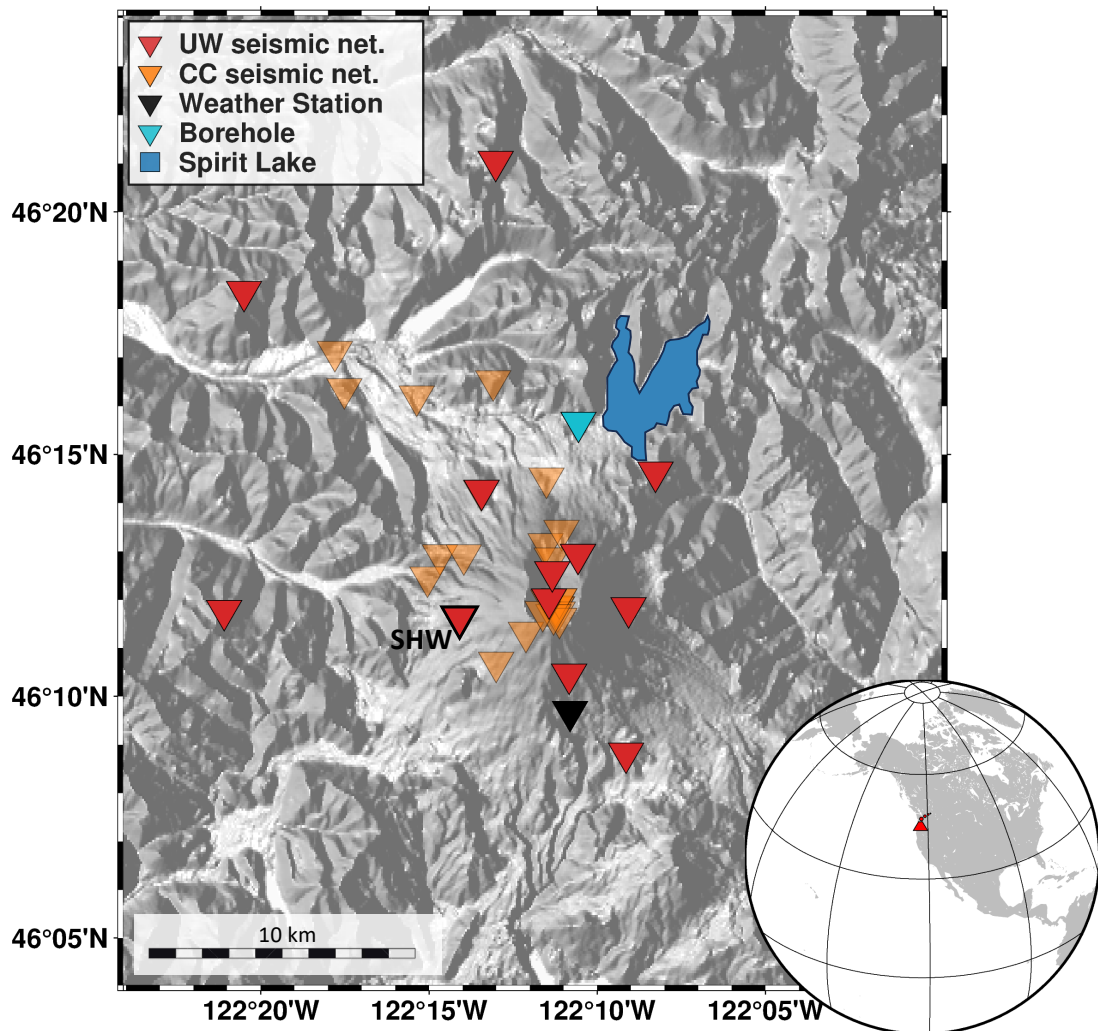


**Figure 1. Station location.** The hillshade of the region around Mount St. Helens with seismic, weather, and borehole stations as inverted triangles. The red triangles mark the short-period seismometers of the UW seismic network (sampling rate: 100 Hz), and the orange triangles mark the broadband seismometers of the CC seismic network (sampling rate: 50 Hz). The black triangle marks the position of the Swift Creek

SNOTEL site at 1350 m.a.s.l. (snow depth data). The bright blue triangle marks the position of the borehole at 1050 m.a.s.l. (water level data). The blue polygon marks the position of Spirit Lake at 1050 m.a.s.l.. The globe at the lower right shows the location of Mount St. Helens in North America. Topography from SRTM [NASA \(2000\)](#).

Various problems arise that affect data quality when gathering data over multiple years and from multiple types of instruments (Fig. S1). For the 2004 eruption, the high instrument density guarantees that there are always data of usable quality. However, the data quality of the individual sensors varies over time. Besides the health of the sensor, the method for the telemetry of short-period seismic data (analog or digital) can add correlated noise and make automated analysis of data quality unreliable. To ensure accurate interpretations, we manually control the data quality before analyzing.

## Methods: Feature Extraction

We used six methodologies dedicated to continuous seismic recordings to analyze Mount St. Helens structural evolution.

The preprocessing (detrending, tapering, and removal of the instrumental response of each day-long time series) remains identical across all methodologies. All features are averaged over the array by stacking or convolving unless otherwise mentioned.

### Statistical Features

We explore standard seismic features, including root-mean-square (RMS), root-median-square (RMeS), peak-ground-velocity (PGV), and peak-ground-acceleration (PGA). These are measured on 10-minute windows seismic data. These features provide statistical and physical interpretation of the seismic wavefield regarding seismic energy and interoperability regarding strains (e.g., velocity) and stresses (e.g.,

accelerations). These measures of ground motions incorporate both a source component (e.g., how energetic the seismic source is) and a structural component (e.g., how attenuative the medium is). We consider RMeS as the metric closest to a noise-level amplitude, RMS a metric close to noise-level but more sensitive to high amplitude signals, and PGV, PGA sensitive to seismic events (unless none occur within the 10-minutes window). This is confirmed by the similar shape of the PGV, PGA time-series (Fig. 3.c) and the 10-minute event rate in Fig. S2, whereas the RMS, RMeS time-series (Fig. 3.d) look slightly different, especially when the inter-event time is long (e.g., earthquake swarm).

#### Real-time Seismic Amplitude Measurement (RSAM)

To compute RSAM, we apply bandpass filters within standard frequency bands used in volcano seismology (2-5 Hz, 4.5-8 Hz, and 8-16 Hz, Tab. S2). These filtered data are segmented into 10-minute windows, from which we extract the time-averaged absolute amplitude (seismic energy). RSAM is low when the site is seismically quiet and high when the site experiences elevated seismicity or seismic noise levels. RSAM can be calculated in real-time and has been used in multiple studies in volcano seismology (e.g., [Endo and Murray \(1991\)](#); [Voight and Cornelius \(1991\)](#); [Ewert and Swanson \(1992\)](#); [Rogers and Stephens \(1995\)](#); [Sherrod et al. \(2008\)](#); [Chardot et al. \(2015\)](#); [Chiodini et al. \(2017\)](#); [Caudron et al. \(2019\)](#); [Dempsey et al. \(2020\)](#)).

#### Displacement Seismic Amplitude Ratio (DSAR)

DSAR is designed as a ratio of low frequency over high-frequency displacement seismograms, correlated with seismic attenuation of the ambient field ([Caudron et al., 2019](#)). Previous studies have chosen 4.5-8 Hz and 8-16 Hz for DSAR after ensuring that these frequency bands were not affected by earthquakes, tremor periods, or sensitive to the evolving microseismic noise ([Caudron et al., 2019](#); [Dempsey et al., 2020](#); [Caudron et al., 2021](#); [Ardid et al., 2022](#)). We chose all three frequency bands used for RSAM and created multiple ratios and proxies for attenuation (Tab. S2). By analyzing the coherence (Fig. S3) and the emitted seismic energy (Fig. S4/S5) of the frequency bands used for DSAR, we find that DSAR can be interpreted as a measure for seismic wave attenuation except for the first year of the eruption. The seismic wavefield at the eruption onset is dominated by events up to 10 Hz.

We also tested a velocity-equivalent (VSAR) that operates on velocity seismograms directly to avoid time-integral displacement for DSAR. Because VSAR and DSAR are proportional to each other (Fig. S6/S7), we continue solely with DSAR for better cross-reference with the literature.

#### Scattering Coefficients

Scattering networks were introduced as inspired by deep learning and multi-scale time series analysis ([Andén and Mallat, 2014](#)). The algorithm constituting a scattering network is a convolutional neural network with banks of wavelet functions as kernel weights. A scattering network of a single layer is equivalent to the wavelet transform. A scattering network of two layers is equivalent to a cepstrum feature but replaces the Fourier transform with a wavelet transform. [Seydoux et al. \(2020\)](#) introduced the algorithms to seismology and found groups of waveforms containing information about the onset of a landslide. These windows of waveforms likely contain seismic events related to the processes without specifically detecting events. Scattering networks do not refer to wave scattering but rather scattering coefficients as products of the convolutions.

The original scattering networks in seismology by [Seydoux et al. \(2020\)](#) used one multi-component seismometer with continuous data as input. We expand on this original formulation to use single-component (vertical), multi-sensor data (8 stations) treated as a single array input.

Before segment-wise convolution of continuous seismic data with wavelets, we apply a highpass filter at 1 Hz and trim the continuous seismic data into 1-minute long time windows with a 50% overlap. This segmentation allows us to discern signals half as long as the window. Wavelets, synthetic waveforms characterized by three parameters — octave, resolution, and quality — play a crucial role in this process. Octave selection hinges on the frequency range of interest,  $f_N/2^{octave}$ , where  $f_N$  is the Nyquist frequency. Resolution aligns with the desired frequency resolution and should be high (dense) for the first layer and low (sparse) for the higher order layers ([Andén and Mallat, 2014](#)). The number of wavelets in a layer equals the product of resolution and octaves. Quality factor gives the information redundancy in the scattering coefficients or, in other words, the width of the peak in the spectral domain. The first layer features a quality factor of 1 and subsequent layers have higher quality factors, preventing wavelet peaks (in the spectral domain) from overlapping, which is essential for envelope modulation evaluation ([Steinmann et al., 2022b](#)). The first layer is set at octaves=4, resolution=4, quality=1, and the second at octaves=5, resolution=2, quality=2. Our wavelet network bank consists of two layers, a configuration validated by [Andén and Mallat \(2014\)](#), who demonstrated that additional layers do not add value. For a detailed discussion of parameter choices for scattering coefficients, we recommend consulting [Andén and Mallat \(2014\)](#); [Seydoux et al. \(2020\)](#); [Steinmann et al. \(2022a,b\)](#).

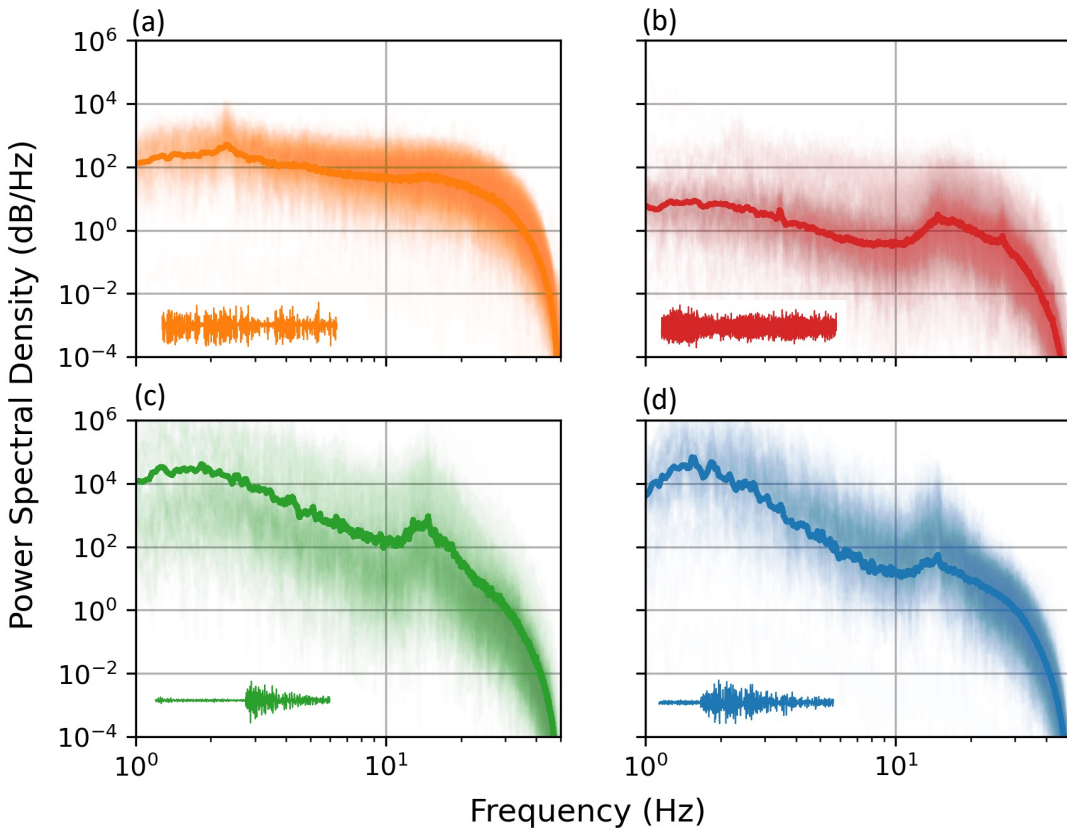


**Figure 2. Power spectral density and example waveforms of the four main clusters.** The thin colored lines represent the power spectrum of random time windows at station SHW belonging to the corresponding cluster where the thick colored line is their mean (found to be similar to their median). The waveform in the lower left corner of each subplot and cluster is an example of a one-minute-long waveform with normalized

amplitude recorded at station SHW. a) Orange cluster - background noise, b) red cluster with increased power at 10-13 Hz but lower low-frequency power, c) green cluster with distinct seismic events with high low-frequency power ( $< 2$  Hz) as well as high high-frequency power (10-13 Hz), d) blue cluster with distinct low-frequency events with high power  $< 2$  Hz (and low power at 10-13 Hz).

Following the wavelet transform, we proceed with temporal downsampling (pooling), offering the option of max pooling or average pooling (Steinmann et al., 2022a). To monitor the stationary background wavefield, we adopt average pooling. The outcome is a high-dimensional feature space, which we subsequently reduce to five features through Independent Component Analysis (ICA). These features are then applied for clustering via k-means using Euclidean distance as the similarity metric. Using the elbow method (Syakur et al., 2018), we find the optimal number of clusters to be 7 (Fig. S8). We only consider 4 out of the 7 clusters because 3 clusters are far apart in feature space (Fig. S9), and contain only a few time windows (Fig. S10/S11).

The seismograms from the four dominating clusters differ in their occurrence, waveform features, and power spectral density (Fig. 2, Fig. S12). The waveforms' shape, especially the relatively flat power spectral density of the first active

cluster (orange), indicates that the cluster contains white and elevated background noise. The second active cluster (red) has a broad peak between 13-15 Hz but also contains background noise, given the lack of impulsive signal in the waveforms and the low power spectral density. This interpretation of the first (orange) and second (red) clusters containing the background wavefield is supported by the high spectral width during that period (Fig. 3). The green (earthquake swarm, tremors, explosion) and blue (associated with dome growing) clusters contain more seismic power, with three times higher power for low frequencies (1 Hz) and a sharp spectral peak at 15 Hz (Waite et al., 2008). The green and blue clusters contain volcanic low-frequency events with different high-frequency content. For example, at 2-10 Hz, the power of the blue cluster waveforms has a steeper falloff ( $f^{-4}$ ) than the green cluster ( $f^{-3}$ ). On the other hand, the high-frequency peak at about 15 Hz is the highest amplitude in the green cluster relative to all other clusters.

## Spectral Width with the Covariance Analysis

The covariance analysis was developed to characterize the diffuse properties of the ambient seismic wavefield of sources located within the array (Seydoux et al., 2016a,b, 2017; Journeau et al., 2020, 2022; Soubestre et al., 2018, 2019, 2021; Caudron et al., 2022b,a). A high spectral (low coherence) widths indicate the times and frequencies of a diffuse ambient seismic wavefield at which diffuse ground vibrations dominate the seismic wavefield. A low spectral width (high coherence) indicates the times and frequencies at which localized seismic sources dominate the seismic wavefield.

For this analysis, we slice the continuous seismic data into 30-second intervals overlapping by 50%, Fourier-transform the short windows, and calculate the cross-coherence for all station pairs and all time windows in the frequency domain. At each frequency, the cross-coherence is a 2D array, with a value for each station pair. To increase the temporal stability of the cross-coherence, we average these matrices over 10 time windows, yielding a final time resolution of 75 seconds (Fig. 4/5/S16) or over 60 time windows giving a final resolution of 450 seconds (Fig. 3). We select the time window length based on the seismic array configuration (e.g., inter-station spacing), the seismic velocity of the region, and the event duration of interest. We then take the singular value decomposition of the symmetric cross-coherence matrix and sort the eigenvalues in decreasing order. Seydoux et al. (2016a) proposed to quantify the eigenvalue spectrum decay with a “spectral width”. A high spectral width implies that many eigenvectors are necessary to reconstruct the wavefield (e.g., a slow decay of the eigenvalues). Therefore, it is characteristic of a complex, multi-scattered, incoherent diffuse wavefield (Seydoux et al., 2016a). Conversely, a low spectral width indicates a low-rank order of the coherence whereby a few or one eigenvectors can reproduce the coherent wavefield (e.g., an incoming plane wave or a single source seismogram simple phase shifted among stations). The analysis also highlights the seismic frequencies in which the ambient field appears stationary or well diffuse, a desirable characteristic for most ambient noise studies (Sánchez-Sesma and Campillo, 2006).

We obtain the most stable results by applying spectral whitening. The spectral width is directly related to the number of stations involved since the rank of the cross-coherence matrix corresponds to the number of stations. The changes in the seismic network over time directly affect the spectral width. To facilitate across-time comparisons of the spectral width during network changes, we normalize spectral width by dividing it by the number of active stations. Our choice of parameterization makes the spectral width more sensitive to long-duration events as it does not detect the

short-duration, distinct volcano-tectonic events observed in raw seismograms (Fig. 4/5/S16).

## Onset of the 2004 Eruption

The following eight subsections describe and discuss the results shown in Fig. 3, where each vertical dotted line marks a seismically or visually observed process. We contrast indicators for seismic activities (RSAM, PGV, PGA, spectral width, cluster activity) with structural change indicators (DSAR). We also show the standard-scaled transformation suggested by Ardid et al. (2022) (Fig. S13/S14). We discuss the evolution of the feature time series averaged over the seismic network. The timeline presented here follows a timeline presented by Moran et al. (2008a), focusing on the confirmed events in 2004.

### Pre-earthquake swarm: before September 23rd

We do not find any significant precursory signals in the ambient seismic field analysis that would indicate aseismic structural changes. The only indication comes with the spectral content of the cluster red waveforms, which, unlike waveforms from the orange cluster, no longer exhibit a white spectrum but also does not exhibit any impulsive signal that would indicate seismicity (Fig. 2/3.f). RSAM, DSAR, and statistical features remain low (Fig. 3.a/b/c/d). The spectral width is stationary, with high levels suggesting a diffuse ambient field (Fig. 3.e).

### Shallow earthquake swarm (I): September 23rd - September 25th 2004

During the shallow earthquake swarm, recognized in real-time as an increasing number of small earthquakes (Qamar et al., 2008), we observe an increase in seismic power across all studied frequency bands (RSAM) (Fig. 3.a), conform with previous findings (Moran et al., 2008a). Complementary to RSAM, the PGV and PGA (Fig. 3.c) increase to moderate values, which we interpret as the increased rate of small seismic events (also present in the PNSN catalog, Fig. S2). However, DSAR (Fig. 3.b), RMS, and RMeS (Fig. 3.d) remain relatively unchanged, which we interpret as a low event rate (3-5 events per minute, Fig. S2). Similarly, the spectral width does not change significantly, except for an increase of the high-frequency content due to the earthquakes (Moran et al. (2008a); Fig. 3.e). Scattering coefficients suggest increased event activity by the appearance of the green event cluster. The coexistence of the green event cluster and the red ambient wavefield cluster aims at a low event rate (Fig. 3.f).

The escalating seismic power, the emergence of an earthquake cluster, and the increased coherence (> 5 Hz) collectively point to Mount St. Helens's known seismic reactivation. This pattern does not suggest aseismic processes, such

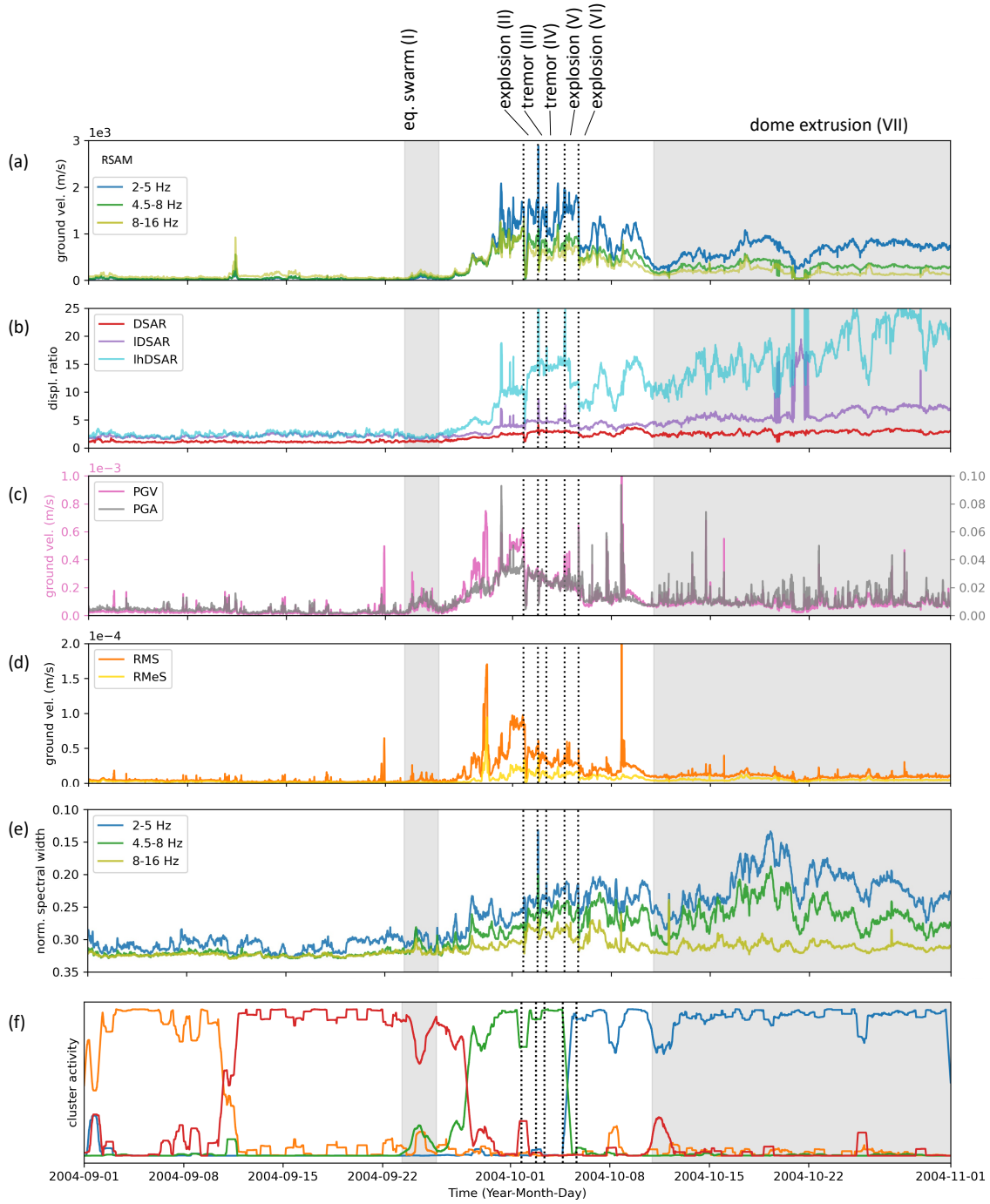


**Figure 3. Onset of the 2004 eruption.** In all subplots, the vertical dotted lines represent the timing of explosions and tremors. The first gray period shows the shallow earthquake swarm, while the second shows the dome growing period. a) RSAM in different frequency bands (2-5 Hz, 4.5-8 Hz, 8-16 Hz). b) Displacement Seismic Amplitude Ratio (DSAR: (4.5-8 Hz)/(8-16 Hz), IDSAR: (2-5 Hz)/(4.5-8 Hz), IhDSAR: (2-5 Hz)/(8-16 Hz)) is a measure proportional to seismic

attenuation. c) PGV and PGA. d) RMS and RMeS. e) Normalized spectral width in the same frequency bands used for RSAM (a). f) Cluster activity, measured as the number of windows belonging to a given cluster smoothed over 4 hours. The orange and red clusters contain ambient seismic noise, and the green and blue clusters contain low-frequency events (< 2 Hz, see Figure 2).

as shallow magmatic intrusion or hydrothermal activities interpreted from DSAR time series at other volcanoes [Ardid](#)

[et al. \(2022, 2023\)](#). Instead, it underlines previous interpretations of magma being in place already before Mount St.

Helens 2004 eruption onset (Moran et al., 2008a) and, therefore, no change in the seismic structure occurs together with the earthquake swarm, suggesting fracturing and sliding in response to increased pressure (Malone et al., 1983; Scott et al., 2008; Moran et al., 2008a; Thelen et al., 2008; Horton et al., 2008).

#### Pre-eruption indicators: September 25th - October 1st 2004

Leading up to the first explosion on October 1st, the RSAM time series showed a rapid increase, particularly in the lowest frequency band (Fig. 3.a). A similar increase can be found for the IhDSAR, IDSAR, and DSAR, although it is less clear due to the plotting axes (Fig. 3.b). PGV, PGA (Fig. 3.c), and RMS, RMeS (Fig. 3.d) increase as well due to the increase in event magnitude and rate. The coherence in the probed frequency bands slightly increases as the spectral width decreases (Fig. 3.e). Additionally, the cluster activity shows a remarkable change, with the green event cluster becoming the dominating cluster (Fig. 3.f), which we interpret as an increasing event rate. At the point where only the green cluster is active, the event rate is around the chosen window length (1 min), confirmed by Moran et al. (2008a).

On September 27th, RSAM, IhDSAR, PGV, RMS, and RMS showed a local maxima caused by wind (Moran et al., 2008a). At the same time, the first co-eruption cracks in the glacier were observed, and the dominant frequency of the earthquakes dropped from 15 Hz to 4 Hz (Moran et al., 2008a), visible in the shift of dominant seismic power and spectral width toward the lower frequencies (Fig. 3). The drop in dominant frequencies may be attributed to the de-

creasing depth of the seismic events (Malone et al., 1983; Moran et al., 2008a; Thelen et al., 2008; Horton et al., 2008), or may originate from resonances in a fluid-filled crack (Crosson and Bame, 1985; Neuberg et al., 2006). As documented by Malone et al. (1983), similar transitions from high to low-frequency events occurred during the 1980–1986 eruptions of Mount St. Helens. They interpreted the frequency shift as upward movement of the event locations due to rising magma increasing stress and causing fracturing and sliding. As magma rose, the events occurred in shallower regions with lower wave-speed materials. The shallow event origin may favor the excitation of low-frequency surface waves, the scattering from material heterogeneity, and topographic effects (Neuberg et al., 2000).

#### 1st explosion & tremor period (II): October 1st

The first explosion of this 2004 eruption occurred on October 1st at 19:02 UTC. It resulted in an immediate and significant drop in RSAM, DSAR, PGV, PGA, RMS, and RMeS (Fig. 3.a/b/c/d), again reaching the pre-explosion level a few hours later. The spectral width briefly drops at the time of the explosion (Fig. 3.e), indicating a short-lived strong coherent source. The cluster activity shifts for a few hours (Fig. 3.f), with the green and red clusters being active.

Before the explosion, elevated seismicity was observed, interpreted as increased pressure in the conduit (Moran et al., 2008a). The explosion released the accumulated pressure, and seismicity (fracturing and sliding) stopped. Approximately three hours elapsed before the seismicity began to increase again, which is interpreted as the time

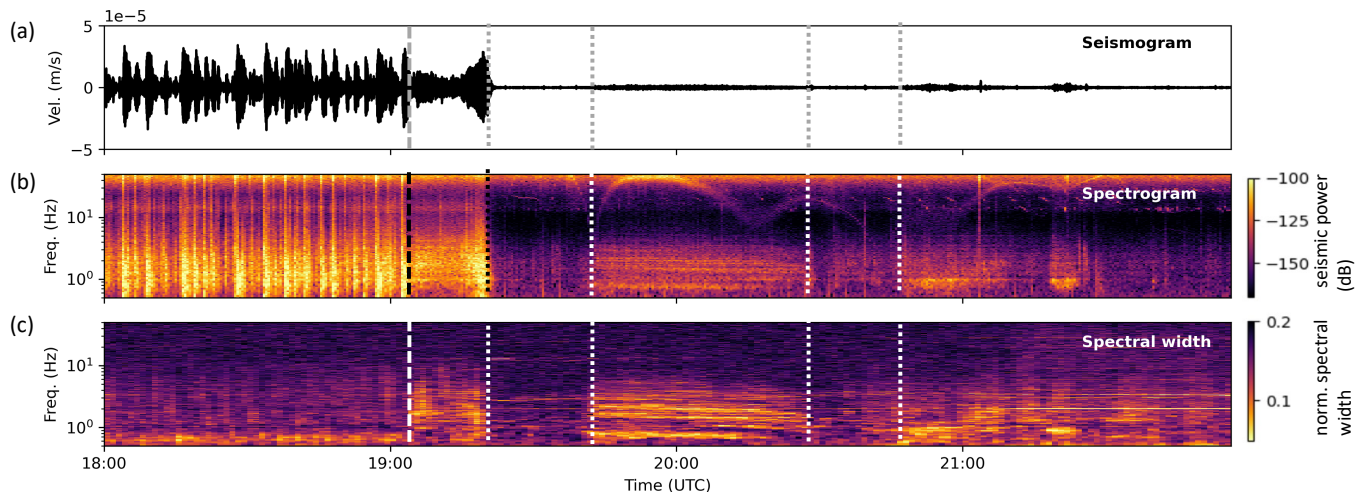


**Figure 4. First explosion on October 1st at 19:02 UTC (vertical dashed line).** a) Seismogram showing 4 hours of data at station SHW, highpass-filtered above 0.5 Hz and downsampled to 50 Hz. b) Spectrogram computed from the data in (a) before downsampling. The bright colors represent

high seismic power. The gliding above 10 Hz is probably caused by helicopters. c) Spectral width of 9 stations computed after applying spectral whitening. Bright colors represent a coherent seismic wavefield (low spectral width).

the system needs to build up enough pressure to enable fracturing and sliding (Aki et al., 1977; Ferrick et al., 1982; Neuberg et al., 2006; Moran et al., 2008a; Thelen et al., 2008). This assumption is supported by both the decline in the green event cluster's activity and the increase in spectral width. While it is unclear whether the change in DSAR was due to source or structural changes, the decrease in spectral width and high amplitude of RSAM favor changes in the seismic source.

The initial explosion was followed by three tremor periods (19:05-19:20 UTC, 19:40-20:25 UTC, and 20:40-22:00 UTC, Fig. 4). For the first tremor period of about 15 minutes, the spectral width analysis supports the interpretation of Moran et al. (2008a) that tremors seemed to occur with a peak frequency of about 2-4 Hz. This followed another 20 minutes of a quiet period and decoherent wavefield. At 19:40 UTC, a tremor period started again and lasted until 20:25 UTC with distinct harmonics at 0.76 Hz, 1.60 Hz, 2.10 Hz and 2.86 Hz that glided down to 0.71 Hz, 1.04 Hz, 1.41 Hz, 1.90 Hz and 2.33 Hz (Fig. S17). The gliding tremor has a fundamental frequency of 0.76 Hz, quite similar to what Dmitrieva et al. (2013) modeled at Redoubt Volcano, with a slight decrease over the 20 minutes, suggesting either a slowing down of the repeated signals or a widening of the cavity. Gliding lines were not reported earlier (Moran et al., 2008a) because they are almost invisible in the spectrogram. The third tremor period resembles the first one with slightly lower dominant frequencies.

### Tremor periods (III & IV): October 2nd & 3rd 2004

Different from the tremors on October 1st, the two tremor periods that occurred on October 2nd & 3rd, coinciding with a peak in RSAM, DSAR, and spectral width, maybe because of a different mechanism or because they are stronger. During the tremor periods, the overall ambient seismic amplitudes (Fig. 3.a) and DSAR are high (Fig. 3.b). PGV and PGA drop during the tremor periods (Fig. 3.c). RMS and RMeS slightly increased during the tremor period and dropped right after (Fig. 3.d). The coherence suddenly rose during both tremor periods (Fig. 3.e), indicating a coherent seismic wavefield dominated by localized sources. No significant change in the cluster activity occurred at that time (Fig. 3.f). The green cluster containing the earthquake swarm remains active. Therefore, we interpret the tremor periods as periods of low-magnitude events, which are no longer distinguishable as discrete events due to the high event rate (Fehler, 1983; Dmitrieva et al., 2013).

A detailed look at the tremor period on October 2nd (Fig. 5) shows that the tremor signal exhibits a distinct signature in a slightly broader frequency band (0.5-10 Hz) and last longer according to the spectral width (19:15-20:30 UTC, Fig. 5.c) compared to measurements from seismic power (0.5-5 Hz, 19:15-20:15 UTC, Fig. 5.b). The period when the tremor signal is observable only through coherence (Fig. 5.c, after 20:15 UTC) corresponds to a narrower coherent frequency band compared to the time when it is also visible through seismic power (Fig. 5.b). The change in the frequency content of the coherent wavefield during the tremor

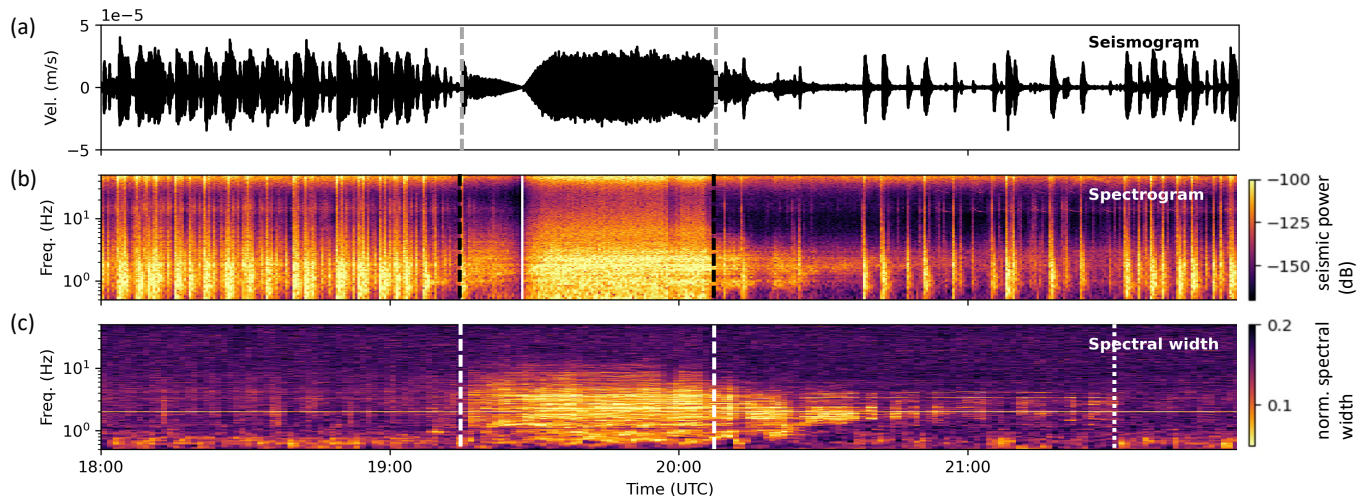


**Figure 5. Tremor episode on October 2nd at 19:15 UTC (vertical dashed line).** a) Seismogram showing 4 hours of data from recordings at station SHW, highpass-filtered above 0.5 Hz and downsampled to 50 Hz. b) Spectrogram computed from the data in (a) before downsampling. Bright colors represent high seismic power. The seismogram (a) and

spectrogram (b) show a high low-frequency event rate before the tremor. c) Spectral width of 9 stations. Bright colors represent a coherent seismic wavefield (low spectral width). The dotted vertical line shows the start and end of the tremor inferred from changes in spectral width.

could result from a dominant event family becoming inactive at the end of the tremor (Thelen et al., 2011). The tremor that occurred on October 3rd is shown in Fig. S16.

#### 2nd explosion (V): October 4th

The subsequent explosion on October 4th differed from that of October 1st with an observed increase in RSAM, DSAR, PGV, RMS, and coherence (Fig. 3). The lowest frequency band (2-5 Hz) shows the most striking increase and is, therefore, clearer on the lhDSAR and IDSAR time series than on the DSAR itself. The cluster activity enters a major transition: the green event cluster (earthquake swarm, tremors, explosion) dies off, and the blue event cluster (associated with dome growing) gets activated.

The behavior of RSAM, DSAR, and coherence at this explosion resembles preceding tremors and explosion. The scattering coefficient analysis reveals noteworthy alterations as the green event cluster gives way to the more complex blue event cluster, suggesting multiple processes going on at the same time. Additionally, the downward vertical displacement motions and changes in the seismic velocity show lasting changes, potentially pointing toward unplugging followed by a pressure release (Makus et al., 2024).

The power spectral density and the peak event frequency analysis by Moran et al. (2008a) indicates events with high power in the lower frequencies (< 2 Hz, drumbeats) for the events during the dome extrusion (blue cluster) but less power for higher frequencies compared to the events during tremor periods and explosions (green event cluster, Fig. 2). It is remarkable that the cluster activity changes so quickly and clearly from a mixture of high and low-frequency events to low-frequency events. This change in event type could signify that this explosion marks the initiation of underground dome formation. It remains unclear why this comparable small explosion could have led to such a fundamental change in volcanic process and event type.

#### Explosion (VI): October 5th

The third explosion led to a drop in seismic power (RSAM) and DSAR, particularly in the lowest frequency band (and therefore lhDSAR). A brief rise preceded the drop in RMS. On the other hand, PGV and PGA were rising during the explosion. The blue cluster is now fully dominating the wavefield. The spectral width decreases in all frequency bands. From this drop in spectral width, we infer a more incoherent wavefield without a single dominating seismic source. With this explosion, the vent-clearing phase concluded as there were no more significant explosions before a new dome formed at the surface (Scott et al., 2008).

#### Post-explosion & Pre-dome building: October 5th - October 11th

The time between the vent-clearing explosions and the onset of dome growth is characterized by fluctuations in RSAM, DSAR, PGV, PGA, RMS, and spectral width (Fig. 3). During that time, the glacier ice and crater floor formed a “welt” pushing up and outward, but no other processes were observed at the surface (Scott et al., 2008). The seismicity was reported to be mostly composed of shallow, relatively low frequency, repeating earthquakes with variable inter-event time that is longer than before October 6th (Thelen et al., 2011), which coincides with our blue cluster seismicity. We suggest that due to the observations of cracks at the glacier and the high activity of the blue cluster, the dome formation is ongoing and started pushing upward.

#### Dome growth period (VII): October 11th and onward

On October 11th, the new dome became visible for the first time (Sherrod et al., 2008). The observed onset of the dome growth period does not manifest any particular pattern in the time series. Large fluctuations are observed mostly at low frequencies of RSAM. DSAR steadily increased after October 11th. PGV, PGA, RMS, and RMeS remained slightly higher than their pre-eruption levels, which is well explained by the overall increase in seismicity during the eruption. The blue cluster remained dominant and also the spectral width for 2-5 Hz and 4.5-8 Hz stays low. We explain this by the occurrence of low-frequency multiples or drumbeats events (Thelen et al., 2008, 2011). At the same time, the coherence of 8-16 Hz returns to the pre-eruption level.

During the dome growth period, we observe an increase in DSAR (Fig. 3.b). The DSAR increase was much more pronounced at stations close to the dome than farther from the crater, which suggests that the perturbation in DSAR is correlated with the dome growth (Fig. S21). An increase in amplitude spectral ratio may be caused by enhanced fracturing during the extrusion of various spines (Vallance et al., 2008), by increased temperature due to the rise of magma (Artemieva et al., 2004; Schneider et al., 2008), or by increased low-frequency seismicity, which seems likely given the spectral width variations. The latter case could not be interpreted as structural change.

### Eruption Period 2004-2008

After exploring the characteristics of the ambient seismic field with six different methods, we interpret the signature of volcanic unrest. We exclude the analysis of the scattering coefficients due to computational constraints of performing ICA over long periods.

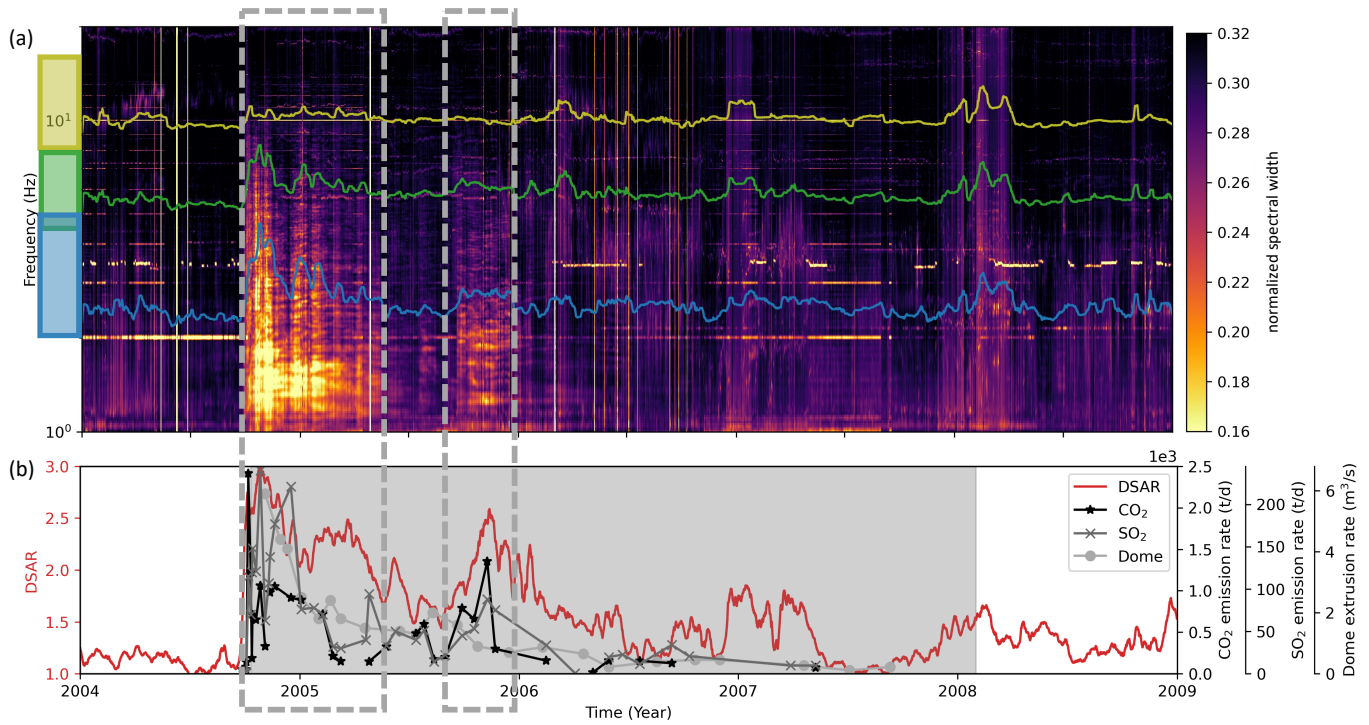


**Figure 6. Spectral width, DSAR, geochemical ( $\text{CO}_2$ ,  $\text{SO}_2$ ), and geodetic measurements.** Two phases of increased volcanic activity are highlighted by dashed gray rectangles, lasting from fall 2004 - summer 2005 and fall 2005 - winter 2005. a) Spectral width in the frequency range from 1 Hz to 20 Hz. The seismic wave field during the active period is more coherent (brighter), especially in frequencies below 5 Hz.

Frequency bands relevant to this study: 2-5 Hz (blue), 4.5-8Hz (green), and 8-16 Hz (yellow). b) Stacked DSAR over the region and three independent measurements of the volcanic activity (dome extrusion,  $\text{CO}_2$ ,  $\text{SO}_2$ ) from Schilling et al. (2008); Gerlach et al. (2008); Dzurisin et al. (2015) show increased values and suggest volcanic activity.

We find two periods (fall 2004 - summer 2005, fall 2005 - winter 2005) of increased coherence at 2-5 Hz (Fig. 6.a) and seismic wave attenuation above 5 Hz (Fig. 6.b). The decay in coherence and wave attenuation during the summer of 2005 correlate with geochemical and geodetic data from Schilling et al. (2008); Gerlach et al. (2008) extended until 2008 by Dzurisin et al. (2015). The second period of enhanced low-frequency coherence and wave attenuation coincided with increases in  $\text{CO}_2$  and  $\text{SO}_2$  emission rates but not with increased seismic energy emission (Fig. S18/S19/S20). This confirms ongoing structural changes as the filling state of the conduit.

The covariance analysis during the 2004-2008 eruption indicates a strong variation in the frequency content of coherent signals, especially in the two periods mentioned above. At the early stages of the eruption (2004-2005), the combination of high coherence and the dominance of the blue cluster, low-frequency earthquakes, in characterizing the ambient seismic wavefield indicates that DSAR is likely related to the change of spectral content of the source whereas later (2005-2008) DSAR (Fig. S13) could be related to structural changes because RSAM (Fig. S10/S11/S12) and

coherence for high frequencies stays low (Fig. 6.a).

Seismic, geodetic, and geochemical measurements may imply an eruption ended already in 2007. However, the ongoing, albeit slowly growing dome, as well as increased seismic activity in winter 2008, led to the definition of the end of the eruption in February 2008 (Scott et al., 2008). The decision was made in July 2008 after five months without any dome growth and seismicity at a normal level.

## Long-term observations

To characterize the non-eruptive background state of the subsurface structure at Mount St. Helens, we deploy the computationally efficient methods for feature extraction over 22 years (Fig. S15) and found that especially DSAR provides insights into seasonal subsurface variations (Fig. 7).

We use the covariance analysis to discriminate the periods and the frequency bandwidth dominated by either a diffuse ambient seismic field or a localized seismic source. Our analysis focused on signals with frequency content above 1 Hz, partly because the covariance analysis indicates large fluctuation in the coherent, non-diffuse ambient field

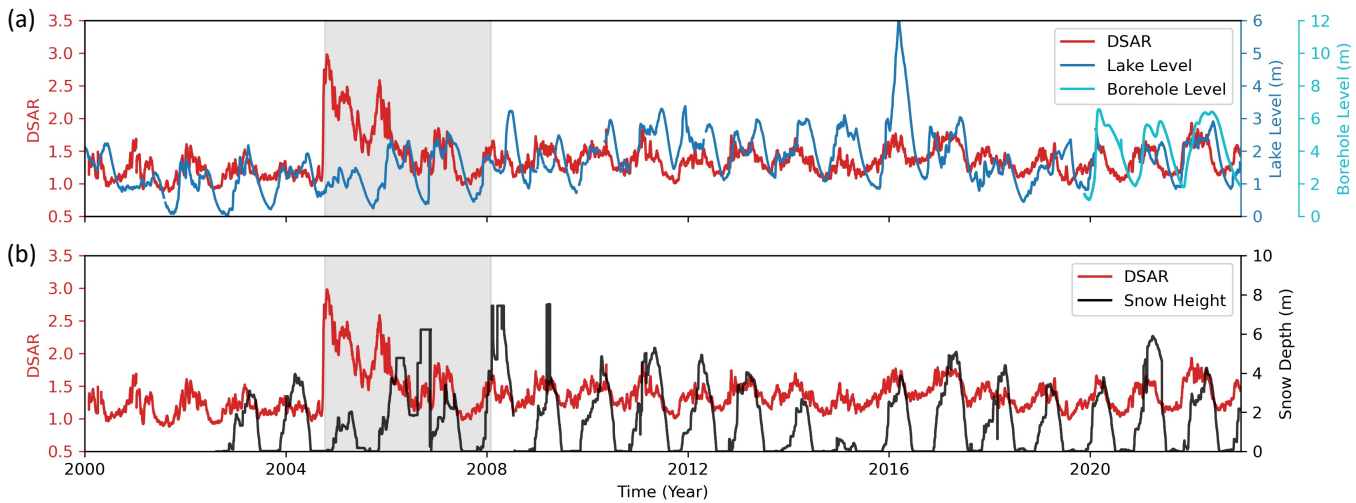


**Figure 7. Comparison between 22 years of seismic attenuation, the water level, and snow height.** 2004-2008 eruption period (gray box). a) DSAR (red), Spirit Lake level

(blue), and a nearby borehole water level (bright blue) show strong seasonal variations. b) DSAR, (red) and snow height (black).

below (Fig. S3), likely an effect of strong microseismic generation in the Pacific Northwest (Tian and Ritzwoller, 2015). The spectral width of specific frequency bands for DSAR does not show a seasonality, which suggests that DSAR observes subsurface changes rather than source changes. Also, DSAR seasonal fluctuations are not correlated with annual variations in RSAM (Fig. S4).

We use 22 years of Spirit Lake level data and 3 years of borehole water level data (locations on Fig. 1). The comparison of the short borehole data with the much longer lake level data shows that both measured water levels follow the same trends with slightly different values (Fig. 7.a). Therefore, we deem it reasonable to use the Spirit Lake level as a proxy for the relative groundwater level, although the lake does have an artificial drainage tunnel. The closure of this tunnel in the spring of 2016 also caused the high lake level at that time (Grant et al., 2017), which provides insights into the natural lake level fluctuations without artificial regulation and shows its similarity in amplitude with the borehole water level.

When DSAR represents the seismic wave attenuation, it can be used to monitor subsurface changes. Also, the seismic velocity change probes subsurface changes and found a similar seasonality (Hotovec-Ellis et al., 2014; Makus et al., 2024) as we observe with DSAR. The borehole water level, lake level, and DSAR, stacked over the seismic stations distributed 18 km around Mount St. Helens smoothing out local effects (Fig. S22), are mostly correlated, with an offset of 3 months between the borehole and DSAR (Fig. 7.a/S22). The shift between seismic data and the water level might

be caused by the location where the individual measurements are taken. The lake and borehole reflect the already infiltrated and stored groundwater. We assume that in addition to the surface water infiltration at depth, the snowpack changes affect the seismic wave attenuation (Fig. 7.b), similar to what Hotovec-Ellis et al. (2014) observed for seismic velocities. Unfortunately, the snow height and borehole water level peak at the same time, which makes it hard to distinguish the effects of snow load and water infiltration. We further note that the DSAR time series at the crater are shaped like crenel functions, with constant values during no snowpack and elevated values during times with a snowpack (Fig. S22.b) or a bit prior to the beginning of the rainfall season. The form changes as a function of elevation (Fig. S22). We interpret the high seismic attenuation as elevated pore pressure due to rainwater infiltration in fall and snow load and snowmelt in a high heat-flux region in winter.

## Conclusion

We conclude that the combination of all methods was essential to disentangle the source from structural effects in continuous ambient field analysis at Mount St. Helens. Using the different methods, we found that the seismic signature during the first year (fall 2004 - summer 2005) of the eruption was dominated by low-frequency sources. Due to the nature of the eruption onset, eruption forecasting using traditional event-based methods at Mount St. Helens was successful. Later (fall 2005), seismic energy emissions were reduced. Therefore, we interpret an increase in DSAR as increased seismic wave attenuation caused by structural changes. This interpretation is supported by geodetic and geochemical measurements. Furthermore, we found a

seasonal pattern in the seismic wave attenuation, correlating with the nearby Spirit Lake level. We interpreted the seasonal seismic wave attenuation as an effect caused by a composite of snow load, water infiltration, and groundwater level.

Overall, the ambient seismic wavefield analysis at Mount St. Helens did not improve the eruption forecasting. However, unsupervised learning showed a change in background noise about two weeks before the first event-based method detected an earthquake swarm. Moreover, before unsupervised learning can be applied as a reliable eruption forecasting method, further investigations on the sources of these newly detected signals have to be done. Neither did further feature extraction as proposed by Ardid et al. (2022) yield additional insights. Nonetheless, the covariance analysis helped unravel source effects from structural effects and enhanced gliding lines during a tremor period embedded between an explosion and two tremor periods without gliding lines.

## Declaration of Competing Interests

The authors declare that there are no competing interests associated with this work. No financial or personal relationships with other individuals or organizations have influenced or could be perceived to have influenced the objectivity, integrity, or impartiality of this research.

## Acknowledgments

We thank Alberto Ardid, Léonard Seydoux, and Cyril Journeau for the interesting conversations and feedback on using their methods. Any use of trade, firm, or product names is for descriptive purposes only and does not imply endorsement by the U.S. Government.

## Data & Resources

The waveform data used in this study are collected by the Pacific Northwest Seismic Network ([University of Washington \(1963\)](#), 10.7914/SN/UW) and the USGS Cascades Volcano Observatory ([Cascades Volcano Observatory/USGS \(2001\)](#), 10.7914/SN/CC). The facilities of EarthScope Consortium were used to access the waveforms, related metadata, and/or derived products used in this study. These services are funded through the Seismological Facility for the Advancement of Geoscience (SAGE) Award of the National Science Foundation under Cooperative Agreement EAR-1724509. The full analysis can be reproduced in [https://github.com/koepflma/MSH\\_AmbientSeismicWavefield](https://github.com/koepflma/MSH_AmbientSeismicWavefield). Additional tables and figures can be found in the supplementary information.

## References

- Aki, K., Fehler, M., and Das, S. (1977). Source mechanism of volcanic tremor: Fluid-driven crack models and their application to the 1963 Kilauea eruption. *Journal of volcanology and geothermal research*, 2(3):259–287.
- Andén, J. and Mallat, S. (2014). Deep scattering spectrum. *IEEE Transactions on Signal Processing*, 62(16):4114–4128.
- Ardid, A., Dempsey, D., Caudron, C., and Cronin, S. (2022). Seismic precursors to the Whakaari 2019 phreatic eruption are transferable to other eruptions and volcanoes. *Nature communications*, 13(1):1–9.
- Ardid, A., Dempsey, D., Caudron, C., Cronin, S., Miller, C., Melchor, I., Syahbana, D., and Kennedy, B. (2023). Using template matching to detect hidden fluid release episodes beneath crater lakes in Ruapehu, Copahue and Kawah Ijen volcanoes. *Journal of Geophysical Research: Solid Earth*, page e2023JB026729.
- Artemieva, I. M., Billien, M., Lévéque, J.-J., and Mooney, W. D. (2004). Shear wave velocity, seismic attenuation, and thermal structure of the continental upper mantle. *Geophysical Journal International*, 157(2):607–628.
- Barajas, A., Journeau, C., Obara, K., and Shapiro, N. (2023). Comparison of continuously recorded seismic wavefields in tectonic and volcanic environments based on the network covariance matrix. *Journal of Geophysical Research: Solid Earth*, 128(12):e2023JB026784.
- Brenguier, F., Shapiro, N. M., Campillo, M., Ferrazzini, V., Duputel, Z., Coutant, O., and Nercessian, A. (2008). Towards forecasting volcanic eruptions using seismic noise. *Nature Geoscience*, 1(2):126–130.
- Cascades Volcano Observatory/USGS (2001). Cascade Chain Volcano Monitoring.
- Caudron, C., Aoki, Y., Lecocq, T., De Plaen, R., Soubestre, J., Mordret, A., Seydoux, L., and Terakawa, T. (2022a). Hidden pressurized fluids prior to the 2014 phreatic eruption at Mt Ontake. *Nature Communications*, 13(1):1–9.
- Caudron, C., Girona, T., Jolly, A., Christenson, B., Savage, M. K., Carniel, R., Lecocq, T., Kennedy, B., Lokmer, I., Yates, A., et al. (2021). A quest for unrest in multiparameter observations at Whakaari/White Island volcano, New Zealand 2007–2018. *Earth, Planets and Space*, 73(1):1–21.
- Caudron, C., Girona, T., Taisne, B., Suparjan, S., Gunawan, H., Kristianto, K., and Kasbani, K. (2019). Change in seismic attenuation as a long-term precursor of gas-driven eruptions. *Geology*, 47(7):632–636.
- Caudron, C., Soubestre, J., Lecocq, T., White, R. S., Brandsdóttir, B., and Krischer, L. (2022b). Insights into the dynamics of the 2010 Eyjafjallajökull eruption using seismic interferometry and network covariance matrix analyses. *Earth and Planetary Science Letters*, 585:117502.
- Chadwick Jr, W. W. and Swanson, D. A. (1989). Thrust faults and related structures in the crater floor of Mount St. Helens volcano, Washington. *Geological Society of America Bulletin*, 101(12):1507–1519.
- Chardot, L., Jolly, A. D., Kennedy, B. M., Fournier, N., and Sherburn, S. (2015). Using volcanic tremor for eruption forecasting at White Island volcano (whakaari), New Zealand. *Journal of Volcanology and Geothermal Research*, 302:11–23.

- Chioldini, G., Giudicepietro, F., Vandemeulebrouck, J., Aiuppa, A., Caliro, S., De Cesare, W., Tamburello, G., Avino, R., Orazi, M., and D'auria, L. (2017). Fumarolic tremor and geochemical signals during a volcanic unrest. *Geology*, 45(12):1131–1134.
- Christiansen, R. L. and Peterson, D. W. (1981). Chronology of the 1980 eruptive activity. Technical Report 1250, US Geological Survey Profecional.
- Crosson, R. and Bame, D. (1985). A spherical source model for low frequency volcanic earthquakes. *Journal of Geophysical Research: Solid Earth*, 90(B12):10237–10247.
- Decker, R. W. (1981). The 1980 activity - a case study in forecasting volcanic eruptions. Technical Report 1250, US Geological Survey Profecional.
- Dempsey, D., Cronin, S. J., Mei, S., and Kempa-Liehr, A. W. (2020). Automatic precursor recognition and real-time forecasting of sudden explosive volcanic eruptions at Whakaari, New Zealand. *Nature communications*, 11(1):1–8.
- Denlinger, R. P. and Moran, S. C. (2014). Volcanic tremor masks its seismogenic source: results from a study of noneruptive tremor recorded at Mount St. Helens, Washington. *Journal of Geophysical Research: Solid Earth*, 119(3):2230–2251.
- Dmitrieva, K., Hotovec-Ellis, A. J., Prejean, S., and Dunham, E. M. (2013). Frictional-faulting model for harmonic tremor before Redoubt Volcano eruptions. *Nature Geoscience*, 6(8):652–656.
- Driedger, C., Neal, C., Knappenberger, T., Needham, D., Harper, R., and Steele, W. (2008). Hazard information management during the autumn 2004 reawakening of Mount St. Helens volcano, Washington. Technical Report 1750, US Geological Survey.
- Dzurisin, D., Moran, S. C., Lisowski, M., Schilling, S. P., Anderson, K. R., and Werner, C. (2015). The 2004–2008 dome-building eruption at Mount St. Helens, Washington: epilogue. *Bulletin of Volcanology*, 77:1–17.
- Endo, E. T., Malone, S. D., Noson, L. L., and Weaver, C. S. (1981). Locations, magnitudes, and statustuccs of the March 20–May 18 earthquake sequence. Technical Report 1250, US Geological Survey Profecional.
- Endo, E. T. and Murray, T. (1991). Real-time seismic amplitude measurement (rsam): a volcano monitoring and prediction tool. *Bulletin of Volcanology*, 53(7):533–545.
- Ewert, J. W. and Swanson, D. A. (1992). *Monitoring volcanoes: techniques and strategies used by the staff of the Cascades Volcano Observatory, 1980–90*. Number 1966. US Government Printing Office.
- Fehler, M. (1983). Observations of volcanic tremor at Mount St. Helens volcano. *Journal of Geophysical Research: Solid Earth*, 88(B4):3476–3484.
- Feng, K.-F., Huang, H.-H., and Wu, Y.-M. (2020). Detecting pre-eruptive magmatic processes of the 2018 eruption at Kilauea, Hawaii volcano with ambient noise interferometry. *Earth, Planets and Space*, 72:1–15.
- Ferrick, M., Qamar, A., and St. Lawrence, W. (1982). Source mechanism of volcanic tremor. *Journal of Geophysical Research: Solid Earth*, 87(B10):8675–8683.
- Frenzen, P. and Matarrese, M. (2008). Managing public and media response to a reawakening volcano: lessons from the 2004 eruptive activity of Mount St. Helens. Technical Report 1750, US Geological Survey.
- Gerlach, T. M., McGee, K. A., and P., D. M. (2008). Emission Rates of CO<sub>2</sub>, SO<sub>2</sub>, and H<sub>2</sub>S, Scrubbing, and Preeruption Excess Volatiles at Mount St. Helens, 2004–2005. Technical Report 1750, US Geological Survey.
- Grant, G., Major, J. J., and Lewis, S. L. (2017). *The geologic, geomorphic, and hydrologic context underlying options for long-term management of the Spirit Lake outlet near Mount St. Helens, Washington*. United States Department of Agriculture, Forest Service, Pacific Northwest ....
- Horton, S., Norris, R., and Moran, S. (2008). Broadband characteristics of earthquakes recorded during a dome-building eruption at Mount St. Helens, Washington, between October 2004 and May 2005. Technical report, US Geological Survey.
- Hotovec-Ellis, A., Vidale, J., Gomberg, J., Thelen, W., and Moran, S. C. (2015). Changes in seismic velocity during the first 14 months of the 2004–2008 eruption of Mount St. Helens, Washington. *Journal of Geophysical Research: Solid Earth*, 120(9):6226–6240.
- Hotovec-Ellis, A. J., Gomberg, J., Vidale, J., and Creager, K. C. (2014). A continuous record of intereruption velocity change at Mount St. Helens from coda wave interferometry. *Journal of Geophysical Research: Solid Earth*, 119(3):2199–2214.
- Jenkins, W. F., Gerstoft, P., Bianco, M. J., and Bromirski, P. D. (2021). Unsupervised deep clustering of seismic data: Monitoring the Ross Ice Shelf, Antarctica. *Journal of Geophysical Research: Solid Earth*, 126(9):e2021JB021716.
- Journeau, C., Shapiro, N. M., Seydoux, L., Soubestre, J., Ferrazzini, V., and Peltier, A. (2020). Detection, classification, and location of seismovolcanic signals with multicomponent seismic data: Example from the Piton de La Fournaise Volcano (la Réunion, france). *Journal of Geophysical Research: Solid Earth*, 125(8):e2019JB019333.
- Journeau, C., Shapiro, N. M., Seydoux, L., Soubestre, J., Koulakov, I. Y., Jakovlev, A. V., Abkadyrov, I., Gordeev, E. I., Chebrov, D. V., Droznin, D. V., et al. (2022). Seismic tremor reveals active trans-crustal magmatic system beneath Kamchatka volcanoes. *Science advances*, 8(5):eabj1571.
- Lipman, P. W. and Mullineaux, D. R. (1981). *The 1980 eruptions of Mount St. Helens, Washington*, volume 1250. US Government Printing Office Washington, DC.
- Machacca-Puma, R., Lesage, P., Larose, E., Lacroix, P., and Anccasi-Figueroa, R. M. (2019). Detection of pre-eruptive seismic velocity variations at an andesitic volcano using ambient noise correlation on 3-component stations: Ubinas volcano, Peru, 2014. *Journal of Volcanology and Geothermal Research*, 381:83–100.
- Maher, S. P., Dawson, P., Hotovec-Ellis, A., Thelen, W. A., Jolly, A., Bennington, N., Chang, J. C., and Dotray, P. (2023). Characterizing and Locating Seismic Tremor during the 2022 Eruption of Mauna Loa Volcano, Hawai'i, with Network Covariance. *The Seismic Record*, 3(3):228–238.
- Makus, P., Denolle, M. A., Sens-Schönfelder, C., Köpfli, M., and Tilmann, F. (2024). Analysing Volcanic, Tectonic, and Environmental Influences on the Seismic Velocity from 25 Years of Data at Mount St. Helens. *Seismological Research Letters*.
- Makus, P., Sens-Schönfelder, C., Illien, L., Walter, T. R., Yates, A., and Tilmann, F. (2023). Deciphering the whisper of volcanoes:

- Monitoring velocity changes at Kamchatka's Klyuchevskoy group with fluctuating noise fields. *Journal of Geophysical Research: Solid Earth*, 128(4):e2022JB025738.
- Malone, S. D. (2020). Recovering Analog-Tape Seismograms from the 1980 Mount St. Helens Pre-Eruption Period. *Seismological Research Letters*, 91(3):1430–1440.
- Malone, S. D., Boyko, C., and Weaver, C. S. (1983). Seismic precursors to the Mount St. Helens eruptions in 1981 and 1982. *Science*, 221(4618):1376–1378.
- Malone, S. D., Endo, E. T., Weaver, C. S., and Ramey, J. W. (1981). Seismic monitoring for eruption prediction. Technical Report 1250, US Geological Survey Profecional.
- Matoza, R. S., Garcés, M. A., Chouet, B. A., D'Auria, L., Hedlin, M. A., De Groot-Hedlin, C., and Waite, G. P. (2009). The source of infrasound associated with long-period events at Mount St. Helens. *Journal of Geophysical Research: Solid Earth*, 114(B4).
- Miller, C. D., Mullineaux, D. R., and Cardell, D. R. (1981). Hazards assessments at Mount St. Helens. Technical Report 1250, US Geological Survey Profecional.
- Moran, S., Malone, S., Qamar, A., Thelen, W., Wright, A., and Caplan-Auerbach, J. (2008a). Seismicity associated with renewed dome building at Mount St. Helens, 2004–2005. Technical Report 1750, US Geological Survey.
- Moran, S. C., Matoza, R., Garcés, M., Hedlin, M., Bowers, D., Scott, W. E., Sherrod, D. R., and Vallance, J. W. (2008b). Seismic and acoustic recordings of an unusually large rockfall at Mount St. Helens, Washington. *Geophysical research letters*, 35(19).
- NASA, J. (2000). SRTMGL1 v003-NASA Shuttle Radar Topography Mission Global 1 arc second. Accessed February, pages 11–21.
- Neuberg, J., Luckett, R., Baptie, B., and Olsen, K. (2000). Models of tremor and low-frequency earthquake swarms on Montserrat. *Journal of Volcanology and Geothermal Research*, 101(1-2):83–104.
- Neuberg, J. W., Tuffen, H., Collier, L., Green, D., Powell, T., and Dingwell, D. (2006). The trigger mechanism of low-frequency earthquakes on Montserrat. *Journal of Volcanology and Geothermal Research*, 153(1-2):37–50.
- Olivier, G., Brenguier, F., Carey, R., Okubo, P., and Donaldson, C. (2019). Decrease in seismic velocity observed prior to the 2018 eruption of Kilauea volcano with ambient seismic noise interferometry. *Geophysical Research Letters*, 46(7):3734–3744.
- Qamar, A., Malone, S., Moran, S., Steele, W., and Thelen, W. (2008). Near-real-time information products for Mount St. Helens—tracking the ongoing eruption. Technical Report 1750, US Geological Survey.
- Rogers, J. and Stephens, C. (1995). SSAM: real-time seismic spectral amplitude measurement on a PC and its application to volcano monitoring. *Bulletin of the Seismological Society of America*, 85(2):632–639.
- Rost, S. and Thomas, C. (2002). Array seismology: Methods and applications. *Reviews of geophysics*, 40(3):2–1.
- Sabra, K. G., Roux, P., Gerstoft, P., Kuperman, W., and Fehler, M. C. (2006). Extracting coherent coda arrivals from cross-correlations of long period seismic waves during the Mount St. Helens 2004 eruption. *Geophysical Research Letters*, 33(6).
- Salzer, J. T., Thelen, W. A., James, M. R., Walter, T. R., Moran, S., and Denlinger, R. (2016). Volcano dome dynamics at Mount St. Helens: Deformation and intermittent subsidence monitored by seismicity and camera imagery pixel offsets. *Journal of Geophysical Research: Solid Earth*, 121(11):7882–7902.
- Sánchez-Sesma, F. J. and Campillo, M. (2006). Retrieval of the Green's function from cross correlation: the canonical elastic problem. *Bulletin of the Seismological Society of America*, 96(3):1182–1191.
- Schilling, S., Thompson, R., Messerich, J., and Iwatsubo, E. (2008). Use of digital aerophotogrammetry to determine rates of lava dome growth, Mount St. Helens, Washington, 2004–2005. Technical Report 1750, US Geological Survey.
- Schneider, D., Vallance, J., Wessels, R., Logan, M., and Ramsey, M. (2008). Use of thermal infrared imaging for monitoring renewed dome growth at Mount St. Helens, 2004. Technical Report 1750, US Geological Survey.
- Scott, W., Sherrod, D., and Gardner, C. (2008). Overview of the 2004 to 2006, and continuing, eruption of Mount St. Helens, Washington. Technical Report 1750, US Geological Survey.
- Seydoux, L., Balestrieri, R., Poli, P., Hoop, M. d., Campillo, M., and Baraniuk, R. (2020). Clustering earthquake signals and background noises in continuous seismic data with unsupervised deep learning. *Nature communications*, 11(1):1–12.
- Seydoux, L., de Rosny, J., and Shapiro, N. M. (2017). Pre-processing ambient noise cross-correlations with equalizing the covariance matrix eigenspectrum. *Geophysical Journal International*, 210(3):1432–1449.
- Seydoux, L., Shapiro, N. M., de Rosny, J., Brenguier, F., and Landès, M. (2016a). Detecting seismic activity with a covariance matrix analysis of data recorded on seismic arrays. *Geophysical Journal International*, 204:1430–1442.
- Seydoux, L., Shapiro, N. M., De Rosny, J., and Landès, M. (2016b). Spatial coherence of the seismic wavefield continuously recorded by the USArray. *Geophysical Research Letters*, 43:9644–9652.
- Sherrod, D. R., Scott, W. E., and Stauffer, P. H. (2008). A volcano rekindled: The renewed eruption of Mount St. Helens, 2004–2006. Technical report, US Geological Survey.
- Soubestre, J., Chouet, B., and Dawson, P. (2021). Sources of volcanic tremor associated with the summit caldera collapse during the 2018 east rift eruption of Kilauea volcano, hawai'i. *Journal of Geophysical Research: Solid Earth*, 126(6):e2020JB021572.
- Soubestre, J., Seydoux, L., Shapiro, N., De Rosny, J., Droznin, D., Droznina, S. Y., Senyukov, S., and Gordeev, E. (2019). Depth migration of seismovolcanic tremor sources below the Klyuchevskoy volcanic group (kamchatka) determined from a network-based analysis. *Geophysical Research Letters*, 46(14):8018–8030.
- Soubestre, J., Shapiro, N. M., Seydoux, L., de Rosny, J., Droznin, D. V., Droznina, S. Y., Senyukov, S. L., and Gordeev, E. I. (2018). Network-based detection and classification of seismovolcanic tremors: Example from the Klyuchevskoy volcanic group in Kamchatka. *Journal of Geophysical Research: Solid Earth*, 123(1):564–582.
- Steinmann, R., Seydoux, L., Beaucé, E., and Campillo, M. (2022a). Hierarchical exploration of continuous seismograms with unsupervised learning. *Journal of Geophysical Research: Solid Earth*, 127(1):e2021JB022455.
- Steinmann, R., Seydoux, L., and Campillo, M. (2022b). AI-Based Unmixing of Medium and Source Signatures From

- Seismograms: Ground Freezing Patterns. *Geophysical Research Letters*, 49(15):e2022GL098854.
- Swanson, D., Casadevall, T., Dzurisin, D., Malone, S., Newhall, C., and Weaver, C. (1983). Predicting eruptions at Mount St. Helens, June 1980 through December 1982. *Science*, 221(4618):1369–1376.
- Syakur, M., Khotimah, B. K., Rochman, E., and Satoto, B. D. (2018). Integration k-means clustering method and elbow method for identification of the best customer profile cluster. In *IOP conference series: materials science and engineering*, volume 336, page 012017. IOP Publishing.
- Thelen, W., Crosson, R., and Creager, K. (2008). Absolute and relative locations of earthquakes at Mount St. Helens, Washington, using continuous data: implications for magmatic processes. Technical Report 1750, US Geological Survey.
- Thelen, W., Malone, S., and West, M. (2011). Multiplets: Their behavior and utility at dacitic and andesitic volcanic centers. *Journal of Geophysical Research: Solid Earth*, 116(B8).
- Tian, Y. and Ritzwoller, M. H. (2015). Directionality of ambient noise on the Juan de Fuca plate: implications for source locations of the primary and secondary microseisms. *Geophysical Journal International*, 201(1):429–443.
- University of Washington (1963). Pacific Northwest Seismic Network - University of Washington.
- Vallance, J., Schneider, D., and Schilling, S. (2008). Growth of the 2004–2006 lava-dome complex at Mount St. Helens, Washington. Technical Report 1750, US Geological Survey.
- Voight, B. and Cornelius, R. R. (1991). Prospects for eruption prediction in near real-time. *Nature*, 350(6320):695–698.
- Waite, G. P., Chouet, B. A., and Dawson, P. B. (2008). Eruption dynamics at Mount St. Helens imaged from broadband seismic waveforms: Interaction of the shallow magmatic and hydrothermal systems. *Journal of Geophysical Research: Solid Earth*, 113(B2).
- Weaver, C. S., Grant, W. C., Malone, S. D., and Endo, E. T. (1981). Post-May 18 seismicity: volcanic and tectonic implications. Technical Report 1250, US Geological Survey Profecional.
- Yates, A., Savage, M., Jolly, A., Caudron, C., and Hamling, I. (2019). Volcanic, coseismic, and seasonal changes detected at White Island (whakaari) volcano, New Zealand, using seismic ambient noise. *Geophysical Research Letters*, 46(1):99–108.

## List of Figures

1	Station locations . . . . .	3
2	Power spectral density and example waveforms of the four main clusters. . . . .	5
3	Onset of the 2004 eruption. . . . .	7
4	First explosion on October 1st at 19:02 UTC. .	8
5	Tremor episode on October 2nd at 19:15 UTC. .	9
6	Spectral width, DSAR, geochemical (CO <sub>2</sub> , SO <sub>2</sub> ), and geodetic measurements. . . . .	11
7	Comparison between 22 years of seismic attenuation, the water level, and snow height. .	12

---

Manuscript Received 12 June 2024